Nuclear Engineering and Technology 57 (2025) 103224

Contents lists available at ScienceDirect

Nuclear Engineering and Technology

journal homepage: www.elsevier.com/locate/net

Original Article

A single-layer compton camera for nuclear decommissioning: An improved back-projection algorithm

Mattias Simons [a,*], Anouk Michiels [a,b], Jan Genoe [b,c], Wouter Schroeyers [a]

[a] Uhasselt – Hasselt University, CMK, NuTeC, Nuclear Technology- Faculty of Engineering Technology, Agoralaan H, 3590, Diepenbeek, Belgium
[b] KU Leuven, ESAT Department, Kasteelpark Arenberg 10 - bus 2440, 3001, Leuven, Belgium
[c] Imec, SAT Departement, Kapeldreef 75, 3001, Leuven, Belgium

ARTICLE INFO

Keywords:
Compton imaging
Gamma camera
Decommissioning
Timepix3

ABSTRACT

The decommissioning of nuclear facilities, a critical and hazardous process due to radiation exposure, necessitates the advancement of radiological measurement techniques concerning safety and efficiency. This study presents an optimized back-projection method, integrating a novel single-layer Compton camera and 3D camera setup with the Timepix3 readout chip to improve the precision and efficiency of gamma-ray source localization in decommissioning scenarios. Implementing 'twin addition' and 'twin multiplication' techniques addressed data ambiguities that arise from event selection in the Compton camera, enhancing the reliability of localization. Introducing a zoom function significantly improved computational efficiency, achieving 163 times faster computation times without sacrificing accuracy. Our method demonstrated enhanced precision with a median angular error of 1.41°, outperforming traditional methods and showing competitive advantages over state-of-the-art technologies, including the Caliste-HD detector. The feasibility of integrating this methodology onto mobile robotic platforms suggests a promising avenue to minimize human radiation exposure and optimize decommissioning tasks, ensuring safer and more effective nuclear facility decommissioning.

1. Introduction

The decommissioning of nuclear facilities presents a significant contemporary challenge. It demands precise identification and characterization of radiation sources, hot spots, and contaminated areas. Traditionally, human operators have undertaken this crucial task, physically entering these facilities and manually conducting measurements [1]. However, this approach comes with a significant drawback—the exposure of operators to potentially harmful radiation. To limit their radiation exposure, the operators are imposed stringent procedural and time constraints, guided by the ALARA (As Low As Reasonably Achievable) principle, to limit their radiation exposure to acceptable levels [2]. While this safeguards workers' health, it concurrently compromises the accuracy and completeness of measurements.

In our pursuit of advancing radiological measurements for decommissioning scenarios, recent developments have demonstrated the transformative potential of integrating technologies such as the Localization and Mapping Platform (LAMP), 3D Scene Data Fusion, and mobile robotics. The LAMP, for instance, has revolutionized real-time, meter-resolution gamma-ray mapping across various applications, from nuclear decommissioning to environmental remediation [3]. This modular sensor suite, capable of being deployed on unmanned aerial vehicles or in man-portable configurations, highlights the importance of remote sensing in safety enhancement and operational efficiency.

Furthermore, integrating mobile robotics into radiological measurement procedures marks a significant leap forward in the methodological arsenal. By leveraging advanced sensing technologies, including LiDAR, these robotic platforms can navigate challenging environments autonomously, collecting and processing data with unprecedented detail and accuracy [4].

These technological advancements underscore a paradigm shift in approaching radiological measurements, moving towards more autonomous, precise, and safe methodologies. This evolution is crucial for the efficient and effective decommissioning of nuclear facilities, furthering our commitment to advancing nuclear safety and environmental stewardship.

Additionally, our prior endeavors [5–8], such as the Archer project [5], have tried to lay a foundational stone in the landscape of nuclear decommissioning research. The archer initiative developed a semi-autonomous robotic platform tailored to characterize

* Corresponding author.
E-mail address: mattias.simons@uhasselt.be (M. Simons).

https://doi.org/10.1016/j.net.2024.09.027
Received 24 May 2024; Received in revised form 31 July 2024; Accepted 21 September 2024
Available online 22 September 2024

decommissioning environments. Central to this platform was deploying a Cadmium Zinc Telluride (CZT) spectrometer, which was instrumental in performing systematic, repeated measurements to map radiation across these challenging settings. The Archer project's innovative approach exemplified the integration of robotic autonomy in radiation mapping and underscored the potential of specialized spectrometry in enhancing the accuracy and efficiency of such measurements.

The deployment of the CZT spectrometer in robotic measurements and optimization of the used method for this spectrometer marked a significant advancement in our ability to conduct detailed radiological assessments. This development of advanced spectrometry and robotic automation exemplifies the forward trajectory of our research, pushing the envelope in the development of safe, efficient, and precise automated methodologies [6–8].

However, this method's time-intensive nature and inherent contamination risk prompted a re-evaluation, replacing the CZT spectrometer with a smaller, lightweight Compton camera developed in previous research [9]. This research, which employed 3D data fusion with LiDAR, is a testament to these technologies' potential in radiation measurements and source localization. The developed measurement approach integrated a single-layer Compton camera with a 3D camera, promising enhanced performance for integration onto a mobile robot facilitated by its lightweight design. This system, leveraging the direct back-projection algorithm, demonstrated its proficiency in pinpointing point sources and estimating activities with a commendable 10 % uncertainty. However, improvements can be made.

The developed Compton imaging system used a direct back-projection algorithm (DBP). This algorithm directly applies Compton kinematics and generates cones of potential source locations by back-projecting each detected gamma-ray interaction onto a spherical surface surrounding the detector. Its advantages lie in its simplicity and intuitive interpretation. However, its limited image resolution with a Full Width Half Maximum (FWHM) of 50 poses a significant challenge. This limitation made distinguishing sources close to each other impossible, highlighting a critical need for improved resolution. Alternative reconstruction algorithms may offer a potential solution to enhance resolution and address this pressing concern.

Another consideration for further research was the event selection criteria for generating a cone. In a single-layer Compton camera, it is often a calculated guess which of the two interactions corresponds to the Compton interaction.

This is in contrast to other methodologies that often prioritize the interaction with the lowest energy as the photoelectric absorption event due to its higher probability following the Klein-Nishina distribution [10]. Additionally, in some scenarios where prior information about the source's location is available, such as in hospital settings, the interaction closest to the front of the detector setup is typically chosen as the Compton scattering event, favoring forward scattering due to its higher probability.

However, our research context differs. In our context, maintaining a four-pi field of view is preferred to maximize the chances of detecting sources, as their locations are unknown. Consequently, in cases where the energy of the interaction prohibits the exclusion of any cones, cones are constructed at both ends of the central axis, acknowledging that this approach may introduce noise into the resulting image. This nuanced approach to event selection balances sensitivity with noise reduction in gamma-ray source localization.

During the development of the Caliste-HD detector as a lightweight Compton camera system, G. Daniel et al. [11] tested four different reconstruction algorithms: (1) Direct Back-projection, (2) Stochastic Origin Ensemble with Resolution Recovery (SOE-RR), (3) a Bayesian algorithm, and (4) a Compton inversion algorithm.

As a result, their study mentioned SOE-RR as a notable algorithm. This algorithm refines the reconstructed image through successive iterations. While computationally demanding, the iterative method demonstrated efficacy in enhancing resolution, making it relevant for precise gamma-ray source localization [12]. This algorithm applies a Monte-Carlo Markov Chain algorithm for Compton imaging, linking each event to a reconstructed image pixel. In each iteration, events transition between pixels based on calculated probabilities. A density map d(x) tracks event counts per pixel. Events randomly choose new positions on the back-projected cone using transition probabilities. The algorithm converges to a stationary state, revealing probable source positions. SOE-RR also introduces Resolution Recovery [13], constructing the back-projection cone randomly based on spatial and spectral resolutions.

The advantages of the SOE-RR method lie in its ability to handle complex spatial and spectral resolutions. However, it comes at a computational cost, as the algorithm requires many iterations for convergence, making the SOE-RR approach particularly well-suited for scenarios where resolution recovery is crucial and computational resources are available [11].

Although such an algorithm might solve our resolution problem, the computational demand poses a significant challenge. As onboard processing can be required for (semi) autonomous robotics operating in complicated decommissioning environments, which might also be busy handling other computations. Despite these algorithms, challenges persist, particularly concerning computational efficiency and adaptability to robotic platforms.

Contrary to an iterative algorithm, G. Daniel et al. [14] recently (2022) introduced a deep-learning algorithm to enhance sensitivity. Their approach involved using a convolutional neural network (CNN) with an architecture adapted from AlexNet. Input for the CNN used a 90x90 image from a direct back-projection representing the solid angles of size 2° by 2°. At the same time, the output was a 45 x 45 image representing the field of view from −90° to 90° discretized in 4° steps. This output image featured a single segment labeled with the source location. Their study showed a promising reduction in the localization error considering the number of events needed, and the computation of the CNN was negligible compared to the DBP algorithm. However, the capacity to handle multiple sources remains unclear. Additionally, it's essential to consider that implementing and training a neural network necessitates comprehensive computational resources. Its suitability for scenarios involving sources other than ^{137}Cs must still be verified.

Contrary to this approach, our research will focus on improving the sensitivity and precision by adapting the direct back-projection method for our single-layer Compton camera to handle the noise introduced by our event selection and overcome computational limitations. Additionally, our research will investigate the improvements made by the 3D reconstruction algorithm discussed in our previous research [9], as the Caliste-HD system did not use this technique. The subsequent sections will delve into the details of our proposed algorithmic enhancements and present a thorough investigation of their performance.

2. Materials and methods

Our previous research [9] focused on developing an experimental lightweight measurement setup tailored for radiological measurements in decommissioning scenarios. This setup comprised two pivotal components: the Compton camera and the 3D camera. The Compton camera played a central role as the primary instrument for detecting gamma rays, enabling the identification and characterization of radiation sources within the environment. Concurrently, the 3D camera provided essential 3D point cloud data of the surroundings, facilitating the linkage of radiological information to its spatial context. Control over the setup's orientation was facilitated by a self-manufactured pan-tilt module equipped with stepper motors and a Raspberry Pi, ensuring precise orientation control and streamlined data acquisition during experimental procedures.

Continuing our research, this established setup will be utilized to conduct further investigations into enhancing the precision and efficiency of gamma-ray source localization. Specifically, we will explore

improvements in the back-projection algorithm, aiming to refine the localization of radiation sources in decommissioning scenarios.

The subsequent sections will delve into the experimental protocols, analytical techniques, and adaptation to the algorithms employed in this study.

2.1. Single-layer compton camera

The Compton camera was designed with a single-layer configuration, combining the functions of both scatter and absorption layers. A 3D reconstruction algorithm determined the distance between coincident events by calculating height differences between coincident interactions. The detector employed a Timepix3 [15] readout chip with a 1000 μm thick CdTe crystal capable of simultaneously registering energy and arrival time in each pixel. More details are displayed in Table 1, and preprocessing steps are described in Ref. [9].

2.2. Event selection

After the measurements, the back-projection maps the data from the detector to the image space. In Compton imaging, cones representing the gamma ray's possible origin can be constructed.

Using Fig. 1 as a schematic representation of a Compton event in the Compton camera. A cone is created with axis *B*A, apex *A*, and angle θ. This cone intersects with a projection sphere, where r is the expected distance from the detector to the source. Typically, when the distance is unknown, r is set to a sufficiently high value, treating it as an infinite radius compared to the detector size. The intersection between the cone and the projection sphere is termed the projection of the cone. This process is repeated individually for each event, and their cones are added to create a back-projection map, with uncertainties influenced by the detector's spatial and spectral resolutions.

The cone's central axis is calculated using the coordinates of the interactions in the detector, and the cone's opening angle is calculated using Equation (1).

$$\cos\theta = 1 - m_e c^2 \frac{E_1}{(E_0 - E_1)E_0} \tag{1}$$

Where θ is the opening angle of the cone, E_0 is the energy of the incident gamma ray, E_1 is the energy deposited in the Compton scattering, m_e is the electron's rest mass, and c is the speed of light.

While Fig. 1 demonstrates the reconstruction of a cone, it relies on knowing the order of interactions—specifically, which interaction represents the scattering of the primary gamma ray and which represents the absorption of the scattered photon. However, when data is obtained from the Compton camera, the order and location of these interactions are initially unknown."

The energy of the scattered photon, E2, is minimal when the photon is scattered at a 180° angle. Equation (2) calculates this energy.

$$E_{2\ min} = \frac{E_0}{1 + \frac{2E_0}{m_e c^2}} \tag{2}$$

Table 1
Characteristics of the Compton imaging system.

Parameter	
Detector	Advapix TPX3
Readout	Timepix3
Number of pixels	256 x 256
Pixel Pitch	55 μm
Crystal materials	CdTe
Crystal dimensions	14 × 14 mm^2
Crystal thickness	1000 μm
Detector weight	503 g
Detector dimensions	25 x 79 × 25.5 mm^3

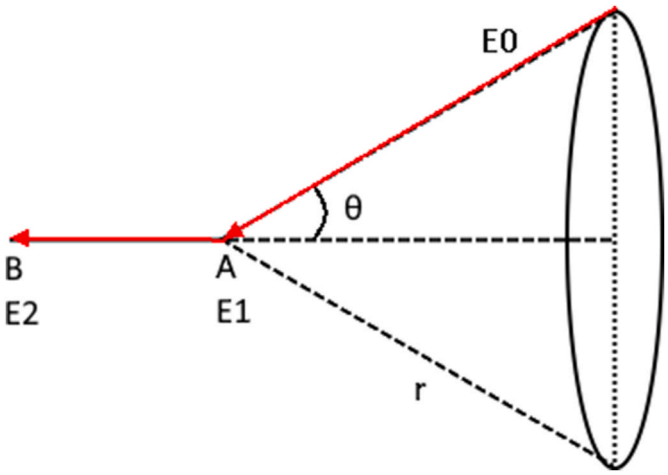

Fig. 1. Schematic representation of a Compton scattering event generating a geometric cone based on detector coordinates and energy measurements. The cone's apex corresponds to the scattering event's location, denoted as A, and its axis extends through the absorption event's coordinates, denoted as B, with the opening angle θ derived from the energies involved, where E1 is the energy deposited in the Compton interaction and E2 in the photoelectric absorption. This model illustrates spatial coordinates and photon energy, which are important in determining the cone's geometry and are pivotal for the subsequent reconstruction of the photon source's location.

When one of the interaction energies is below the minimal energy E_{2min} of a Compton scattered photon, the order of interactions can be determined. However, when both interaction energies are larger than E_{2min}, it is impossible to determine the order of the interactions a priori. In such cases, cones are constructed at both ends of the central axis, which we will later introduce as 'twin cones.'

2.3. Direct back-projection

After the measurement and creation of cones, they are back-projected following the approach described in Fig. 2. In our research, a spherical projection surface is used. It is assumed that the dimensions of the detector are negligible compared to the sphere's radius.

Fig. 2 shows the flowchart of our back-projection algorithm for a single cone involving several steps. An example of a theoretical cone with a central axis $\rightarrow u = [1,0,0]$ and an opening angle $\theta = 45°$ is used to illustrate each step.

Fig. 3 illustrates the parameterization and discretization of the projection sphere into sphere segments using the elevation and azimuthal angles. An array corresponding with the unit vector of each sphere segment is created.

Next, Fig. 4 shows how the angular difference δ_{axis} between the cone's axis and each point on the projection sphere is calculated.

Then, Fig. 5 shows the opening angle of the cone is subtracted from the angular difference, and the magnitude of the array is calculated δ_{cone}.

Subsequently, a Gaussian function (Equation (3)) is applied to the matrix to assess the likelihood of the cone going through this section of the sphere based on Gaussian overlap δ_g, resulting in Fig. 6.

$$\delta_g = e^{\frac{-(\delta_{axis}-\theta)^2}{2\sigma^2}} \tag{3}$$

Finally, the 2D array with Gaussian overlap is summed with the results from previous cones, and this process is repeated for each cone.

2.4. Twin addition

In our methodology, the scenario is encountered where two cones are constructed from a single set of interactions (Compton scattering and

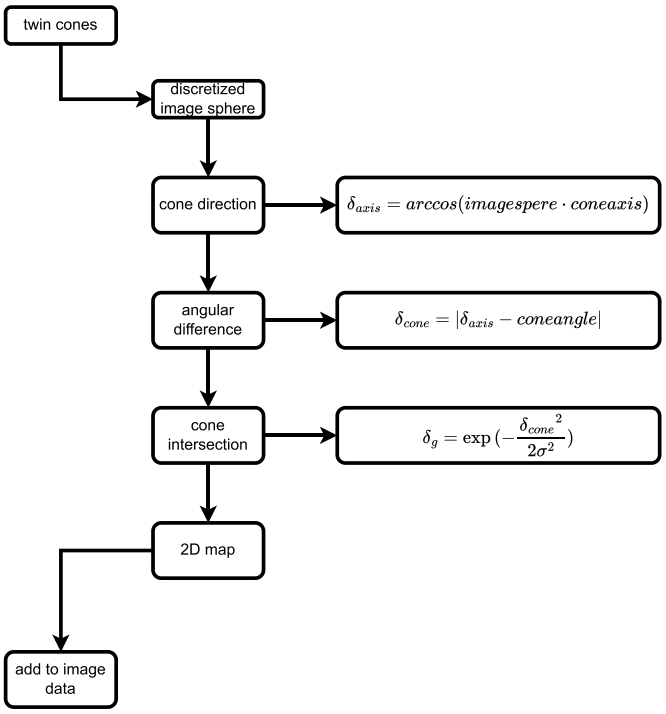

Fig. 2. Flowchart of the Back-projection process for a Compton Camera. Starting from a cone axis and opening angle, the algorithm calculates the angular difference between the cone axis and a discretized image sphere, subtracts the opening angle, and applies a Gaussian intersection operator to create a 2D map. This map is incrementally added to the cumulative image data, representing one cone of the reconstruction algorithm.

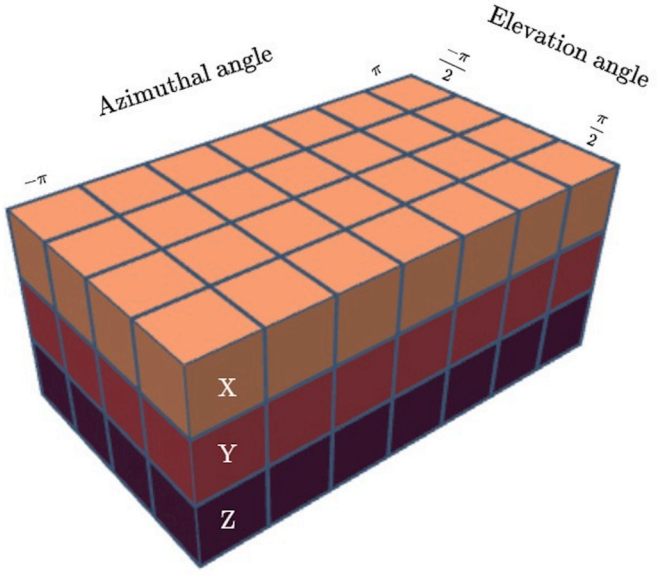

Fig. 3. 3D Matrix representation of a discretized projection sphere. The grid-like structure visualizes the parameterization of the sphere into distinct volumetric elements, facilitating the quantitative analysis of data within a 3D space. Each voxel represents a discrete sphere segment with associated values, as indicated by the varied colors, aligned along the Cartesian coordinates X, Y, and Z, with the Z-axis emphasizing the matrix's depth dimension. (For interpretation of the references to color in this figure legend, the reader is referred to the Web version of this article.)

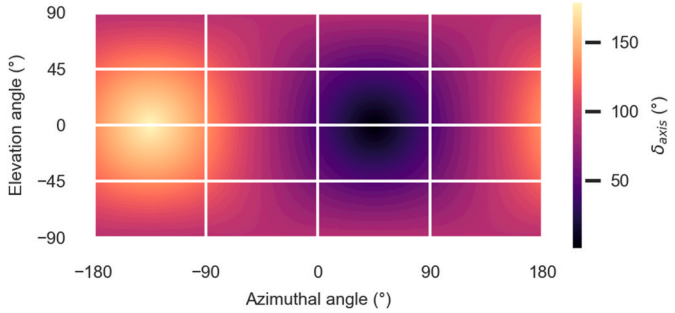

Fig. 4. Heatmap visualization of the angular difference δ_{axis} distribution in the initial back-projection step for a Compton camera. The color gradient represents the angular difference, with each point corresponding to the angular dispersion relative to the cone's axis. (For interpretation of the references to color in this figure legend, the reader is referred to the Web version of this article.)

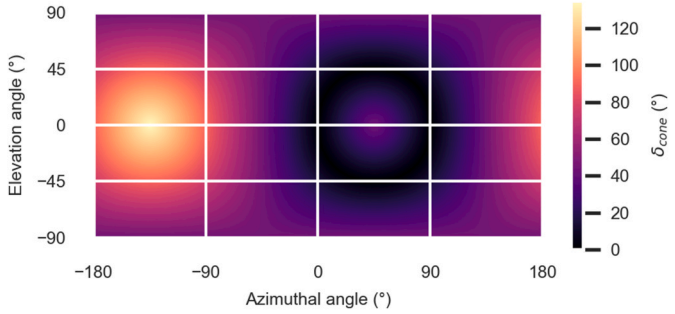

Fig. 5. Heatmap visualization incorporating the cone angle in the algorithm for Compton camera imaging. This representation shows the magnitude of the angular differences between the cone's intersection and the sphere segment. Each color gradient shift signifies a variation in intensity mapped against the cone geometry. (For interpretation of the references to color in this figure legend, the reader is referred to the Web version of this article.)

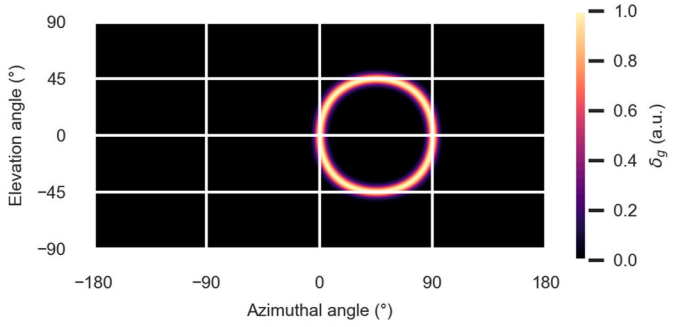

Fig. 6. Heatmap visualization of Gaussian overlap δ_g between the Compton scattering cone and the projection sphere in the final step of the algorithm. This representation quantifies the likelihood of source locations on the projection sphere, employing a color-coded scheme to indicate probability levels derived from Gaussian distribution models. This image marks areas of maximum likelihood to contain the source. (For interpretation of the references to color in this figure legend, the reader is referred to the Web version of this article.)

photoelectric absorption). A cone is then generated at both sides of the central axis, and the respective event's energy determines the cone's opening angle. This is what will be introduced as 'twin cones.'

In our previous research [9], these twin cones were separately added to the back-projection algorithm. However, by doing this, not all information is considered. It is known that these two cones are generated from the same event. Instead of adding 2D maps of the individual cones

separately, we introduce 'twin addition' to acknowledge that these twin cones represent a single event. This method preserves the information about the simultaneous generation of both cones. A refined 2D map that contains the maximum of the maps from both individual cones is made, and this map is, in turn, added to the result. This process is shown in the flowchart in Fig. 7.

The significance of this method becomes evident in its ability to mitigate potential issues arising from (partial) overlapping twin cones. Adopting the maximum value for each point avoids the risk of considering overlapping points as double hits, thereby minimizing the impact of noise caused by the faulty twin cone in the localization process.

This 'twin addition' technique ensures a more accurate representation of the origin of the gamma-ray source, contributing to the overall reliability of localization results.

2.5. Twin multiplication

In the previous section, 2D maps are added together. Theoretically, with a single point source, a perfect detector, and without background radiation or other interference, all cones should overlap in a single pixel in the 2D map. Instead of adding, it should be possible to multiply all 2D maps.

However, a wrongfully picked cone could mean the entire result is multiplied by a very small number or zero. In this method, it is necessary to use the principle of twin cones to limit the influence of faulty cones from picking the wrong side of the interaction and multiplying the array by zero.

However, a more favorable alternative is to compute the natural logarithm of δ_g (equation (3)). Besides producing numbers whose absolute value is greater than 1 (in most cases), it provides two other advantages. First, the natural logarithm is the inverse of the exponential function, which means they cancel each other out (equation (4)). Second, by taking the natural logarithm, the multiplication of 2D maps changes into addition as ln(a· b) = ln(a) + ln(b), making it less computationally expensive.

$$\delta_m = ln(\delta_g) = \frac{-|\delta_{axis} - \theta|^2}{2\sigma^2} \tag{4}$$

Another difficulty is the influence of faulty cones from other sources, such as background radiation. When these cones arise, the result is multiplied by a small number, and when this is repeated often, it will reach the computational limits and become zero. Therefore, a cutoff value v_c is introduced. Resulting in Equation (5).

$$\delta_{m,c} = \begin{cases} \delta_m, \delta_m < \ln(v_c) \\ \ln(v_c), \delta_m \geq \ln(v_c) \end{cases} \tag{5}$$

2.6. Zoom function

Additionally, a zoom function is implemented. This function is pivotal in optimizing the computational efficiency by limiting the required matrix calculations. This process involves a strategic series of steps. Initiated by a back-projection using a projection sphere with reduced accuracy, the result is then analyzed to calculate a point of interest (P_c). Subsequently, a square raster with enhanced accuracy centered around P_c is created. This new focused region of interest is subjected to further back-projection for every point within the raster, allowing for targeted computations and refined accuracy. Illustrated in Fig. 8, the zoom function showcases the concept's practical application. The zoom function achieves the same accuracy as direct calculations but significantly faster by limiting the required matrix calculations. Importantly, this method can be iteratively employed and offers a flexible approach towards the desired accuracy.

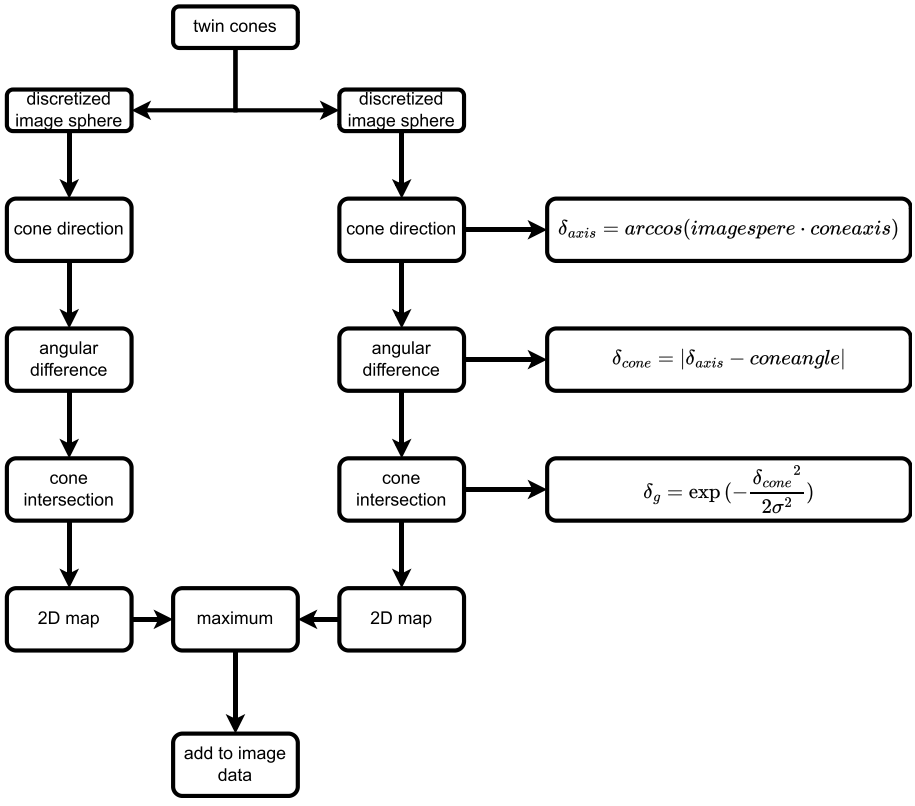

Fig. 7. Flowchart of the adapted twin addition algorithm. When possible, the process generates two cones for each set of detected events, calculates their Gaussian overlaps with the image sphere, and selects the maximum value from both possibilities at each point.

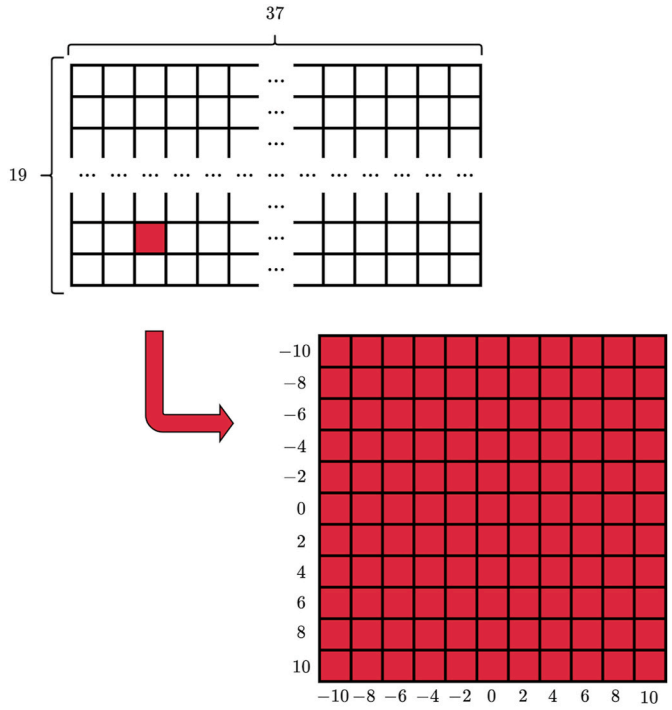

Fig. 8. Zoom-in process on a 2D projection sphere for Enhanced Resolution. The upper diagram displays the original map with a broader accuracy. As shown in the lower diagram, the pixel of interest is identified and expanded into a finer-resolution map centered on the pixel of interest from the original grid. This process allows for a higher accuracy projection on the sphere, narrowing down to a specific region for detailed analysis.

2.7. Computation time

As computational demand is an essential issue in our use case, a comparative analysis assesses the computational efficiency of various methods, and the processing times are calculated for each method.

The computations are performed for a specific measurement scenario where a ^{137}Cs source (14.15 MBq) was located at [−15.3° elevation, −4.95° azimuthal]. This source was measured for 60 min at 30 cm distance. The preprocessing steps, such as event selection, are the same for all methods. Therefore, computation times start from precomputed angles, axes, and projection sphere.

It is crucial to emphasize that the processing time solely accounts for the time required to perform the back-projection algorithm. To ensure time readings, the time. process_time function is employed. The set of calculations is conducted five times with subsequent averaging. Our research uses a MateBook 14 with an intel® core™ I7-10510u CPU and 16 GB of RAM to measure computation time.

However, notable fluctuations in compute time were noticed when repeating the process, even using the time. process_time function. Such variability arises due to inherent computer state differences during each calculation. Despite these variations, the absolute calculation times are less crucial than the relative ratios observed at approximately the same moment.

Also, the effectiveness of the zoom function is systematically assessed through tests with varying settings to identify optimal parameters (number of iterative steps and accuracy in each step). The objective is to measure the impact on processing time and ascertain the configurations that result in the most significant reduction in computational load.

2.8. Experimental setup

A dataset of measurements under different incident angles is gathered to assess our imaging system's and algorithms' performance. Acquisitions are conducted to generate a dataset of measurements at 5° intervals across the field of view, ranging from (and including) −55°–55° in elevation and azimuthal angles. This resulted in 529 acquisitions, each consisting of a 1-h measurement with a ^{137}Cs hotspot positioned 30 cm from the detector.

To create an error distribution analysis, the angular error is calculated as the difference between the location corresponding to the maximum in the back-projected heatmap and the true location of the source. This process is repeated for an increasing number of events for each measurement orientation in the dataset. The ^{137}Cs hotspot consisted of four ^{137}Cs sources located directly behind each other for a combined activity of 14.15 MBq ± 5 %.

The positioning precision of the radiation source was characterized by an uncertainty of approximately 1° for both azimuthal and elevation angles and 3 mm for the distance between the sources and the detector.

3. Results

This section presents the results of the optimized back-projection method, assessing precision and accuracy for each step. Initially, the discussion revolves around utilizing the Timepix3 as a Compton camera without additional computation or algorithms, establishing a baseline. Subsequently, each step of our optimized back-projection method is introduced sequentially, and the results are analyzed.

This systematic evaluation aims to gauge the influence of each step on gamma-ray source localization precision and computational resource utilization. The findings offer insights into the effectiveness of the optimized approach compared to the baseline method.

3.1. Baseline results

This section presents the outcomes of utilizing the Timepix3 as a Compton camera without additional computation or algorithms, including no 3D reconstruction. This method's precision and computation time are reference points for comparison with the optimized back-projection techniques introduced later in the study.

The Point Spread Function (PSF) is plotted in Fig. 9 and fitted by a Gaussian function. This was done for the measurement with the source at 0° azimuthal and 0° elevation angle. This PSF displayed non-Gaussian characteristics. However, when fitted, it exhibited a Full Width at Half Maximum (FWHM) of 90°. This analysis sheds light on the spatial distribution and resolution of the gamma-ray source localization without incorporating 3D reconstruction.

Without 3D reconstruction, distinguishing between the front and back of the detector was impossible due to the lack of height

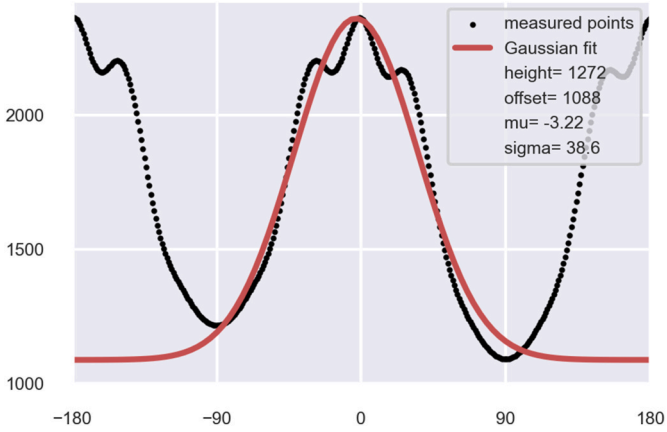

Fig. 9. The point spread function (PSF) for the baseline back-projection method without the inclusion of additional 3D reconstruction data. The PSF is visualized to assess the method's spatial resolution capabilities and effectiveness in accurately representing point sources.

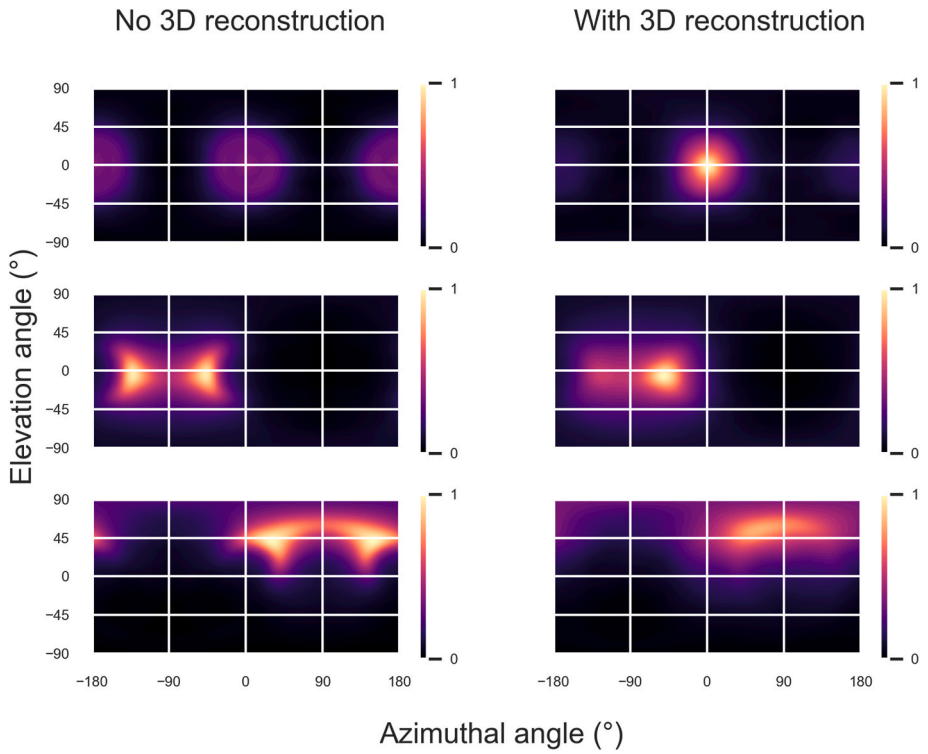

Fig. 10. Side-by-side heatmaps comparing the results of three distinct measurements analyzed using the baseline back-projection method and its enhanced counterpart with additional 3D reconstruction data. Each heatmap illustrates detected signals' spatial distribution and intensity, allowing for a direct visual comparison of method efficacy in spatial resolution. For the top measurement, the source was located at [0° elevation, 0° azimuthal]; for the middle measurement, the source was located at [-5° elevation, −50° azimuthal]; and for the bottom measurement, the source was located at [50° elevation, 50° azimuthal].

information, and all interactions are located on the xy plane. This resulted in the image being mirrored across the xy plane, causing the mirrored image across the −90° and 90° azimuthal angle line visible in the PSF in Fig. 9. Additionally, to illustrate this in Fig. 10, three measurement orientations are provided as examples. Consequently, the field of view had to be restricted to 180°.

To compare our baseline with the other proposed algorithmic enhancements, the field of view is limited to 180°. Fig. 11 shows the error distribution analysis that displays the angular error for increasing event numbers. The figure shows that longer measurement times or more events lead to a lower angular error; however, the descent is slow. After

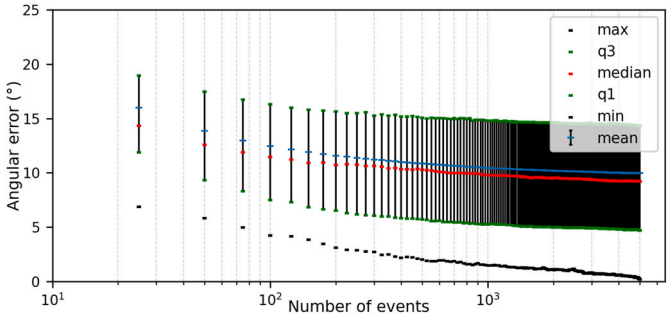

Fig. 11. Error Distribution Analysis for the baseline result. Back-projection without 3D reconstruction with variable event counts. This scatterplot showcases the distribution of angular errors for the baseline result, utilizing a dataset of 529 measurements across varying numbers of events. The y-axis represents the error magnitude, while the x-axis indicates the number of events used in the back-projection process. Key statistical metrics, including minimum, first quartile (Q1), median, mean, third quartile (Q3), and maximum error, are depicted, providing a comprehensive overview of the method's performance. Note that maximum errors are not shown on the plot as they are too high to fit the scale.

3000–3500 events, the mean error stagnates at 9.96°, while the median error stagnates at 9.25° error. However, the worst-case error (maximum) stagnates at 27.5°.

3.2. Optimized back-projection methods

After establishing the baseline in the previous section, this section examines the results of implementing the adapted back-projection techniques. First, the outcomes of employing 3D reconstruction alongside back-projection are discussed, and its impact on precision is assessed. Subsequently, the results of applying back-projection using the twin addition and twin multiplication methods are explored, analyzing their effectiveness in improving gamma-ray source localization. Through this comprehensive evaluation, the strengths and limitations of each optimized approach are elucidated compared to the baseline method.

3.2.1. Back-projection with 3D reconstruction

When adding the 3D reconstructed z coordinate to the events, it becomes possible to distinguish between the front and back of the detector. Fig. 10 shows the three examples of measurements with different orientations. When using 3D reconstruction, it is possible to determine the side of the detector where the source is located. However, 'noise images' often appear mirrored across the 90° azimuthal line, but the mirrored image at a 180° azimuthal angle in the PSF Fig. 12 is reduced compared to the results without 3D reconstruction (Fig. 9). Therefore, the field of view is increased again to 360°.

Fig. 12 shows the PSF with this reconstruction algorithm. This PSF matches the Gaussian fit better than the previously discussed baseline. It also shows that the FWHM of the angular resolution improved to 49°.

Fig. 13 shows the error distribution analysis for the back-projection with 3D reconstruction. Initially, the median error decreases significantly as the number of events increases. Starting from a median error of

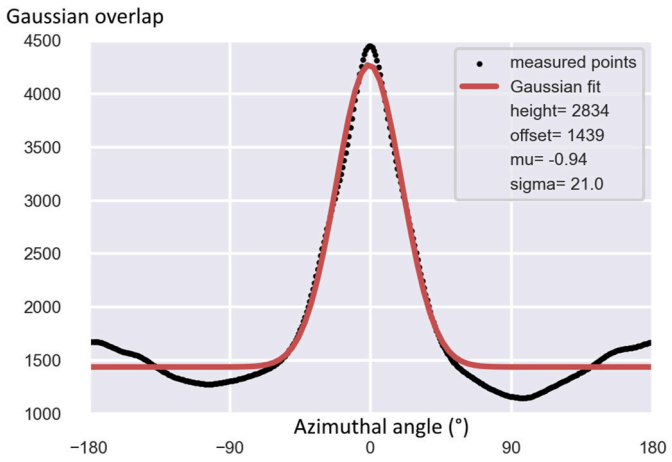

Fig. 12. Point Spread Function with Incorporation of 3D reconstruction data. This figure showcases the PSF when employing the enhanced back-projection method that includes additional 3D reconstruction data.

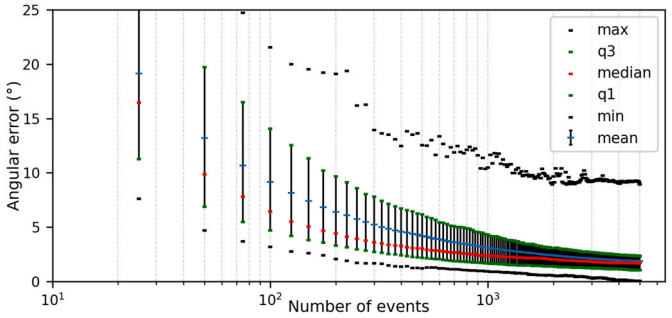

Fig. 13. Detailed Error Analysis for adapted back-projection with 3D reconstruction with increasing events. This scatterplot details the angular error distribution for direct back-projection with 3D reconstruction, utilizing a robust dataset of 529 measurements as the number of events for the back-projection algorithm increases. On the y-axis, angular error metrics are depicted to assess the method's precision, including the minimum, first quartile (Q1), median, mean, third quartile (Q3), and maximum values.

16.44° at 25 events, it falls to about 3.03° at 500 events. As the number of events continues to increase, the decrease in median error slows down. From around 1000 to 5000 events, the median error values show a much slower decrease, stabilizing around 1.68°. Although the maximum angular error does not decrease much after 1000 events and stagnates at about 9.2°, the interquartile range decreases, meaning that increasing the number of events leads to more consistent measurement errors, reducing the variability among most of the angular errors.

3.2.2. Twin addition

This algorithm, characterized by its methodology of incorporating twin events, demonstrates slight further improvements in angular error. This section delves into assessing the twin addition algorithm's efficacy, precision, and overall performance in gamma-ray source localization tasks.

When adding our twin algorithm, Fig. 14 shows an error distribution analysis similar to that seen in Fig. 13. However, there is a slight improvement in the angular error at lower numbers of events.

The median error decreases rapidly from high initial values as the number of events increases from 15.7° at 25 to 2.79° at 500 events. This suggests significant improvements in accuracy with the initial addition of more data points.

After reaching approximately 1000 events, the curve starts to flatten, indicating that the median error does not improve much with adding more events. The decrease slows down and stagnates at 1.56°.

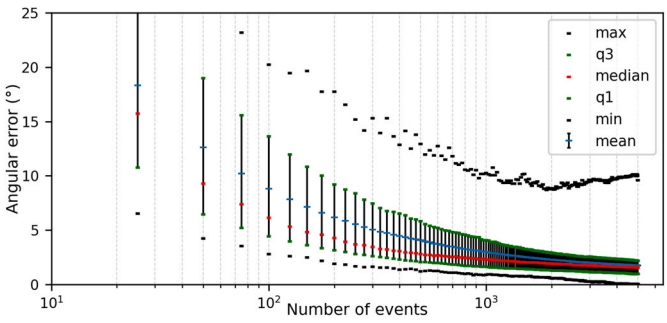

Fig. 14. Angular error distribution for adapted back-projection "twin addition" by event count. This scatterplot illustrates the angular error distribution for twin addition, analyzed over a dataset of 529 measurements with an incrementally increasing number of events. The y-axis delineates various statistical measures of angular error (minimum, first quartile (Q1), median, mean, third quartile (Q3), and maximum), offering insight into the method's accuracy over time.

Like the median error trend, the interquartile range (IQR) begins to level off as the event count reaches higher values, particularly around 3000 to 3500 events. Beyond this point, the decrease in IQR becomes much more gradual, suggesting that the variability among the majority of the data points stabilizes and does not improve significantly with additional data stagnating at 1.23°.

3.2.3. Twin multiplication

Upon implementing the twin multiplication algorithm, our analysis reveals another nuanced improvement in angular error reduction compared to twin addition. The algorithm's core principle—leveraging the concurrence of twin events to multiply probabilities—results in a more stringent selection criterion for potential source locations. However, instead of a 2D heatmap, as in Fig. 10, this methodology displays a single brightly lit pixel pinpointing the most probable source location.

Fig. 15 shows the efficacy of the twin multiplication approach, it is best observed through a detailed statistical analysis of angular resolution. Similar to the error distribution plots discussed in Figs. 14 and 13, the median error sharply decreases as the number of events increases from 14.1° at 25 to 2.88° at 500. A decreasing IQR indicates the algorithm's robustness in pinpointing a single location of a point source.

3.3. Comparison with baseline

This section compares the precision and computation time of the

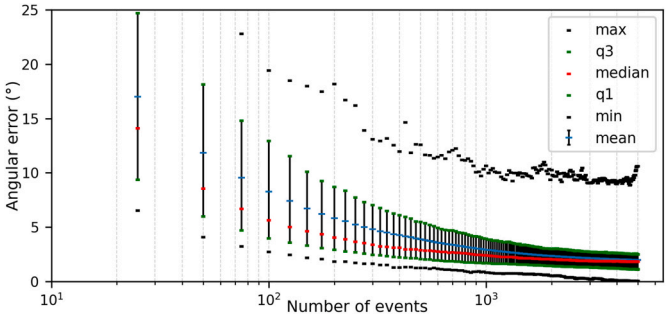

Fig. 15. Evaluation of angular error for adapted back-projection "twin multiplication" as a function of event count. This scatterplot displays the angular error for twin multiplication, using the dataset of 529 measurements while progressively increasing the number of events. To evaluate the method's precision, the y-axis plots statistical indicators of angular error—including the minimum, first quartile (Q1), median, mean, third quartile (Q3), and maximum values.

optimized back-projection methods with those of the baseline approach. This elucidates the optimized techniques' efficacy in enhancing gamma-ray source localization performance. This comparative assessment of precision and computation time is performed among the optimized back-projection methods (Back-projection with 3D reconstruction, twin addition, and twin multiplication).

The error distribution analysis of the three improved algorithms exhibits similarities, indicating comparable performance. A comparative analysis focused on the median angular errors with increasing events, as the median angular error provides a concise yet comprehensive metric to assess each method's performance. Fig. 16 illustrates that plotting the median errors against the number of events allows us to observe distinctive patterns.

In assessing the angular error across varying event counts for the four distinct algorithms, findings revealed that algorithm twin multiplication consistently registered the lowest angular errors, showcasing its superior precision. Specifically, at an event size of 500, algorithm twin multiplication recorded an angular error of 2.89°, closely followed by twin addition and back-projection with 3D reconstruction with errors of 2.79° and 3.03°, respectively, indicating that their performances were nearly comparable to twin multiplication. Notably, twin addition slightly surpassed back-projection with 3D reconstruction by achieving an error rate of approximately 3 % lower than twin multiplication. In contrast, the baseline results exhibited substantially larger angular errors, about 3.56 times greater than twin multiplication at the same number of events. This significant difference underscores the relative imprecision of the baseline results and highlights the comparative accuracy of the other algorithms, especially the twin algorithms.

Twin addition is the best performer at higher event counts (upper 25 % of data), with the lowest average angular error of approximately 1.61°. This demonstrates that twin addition maintains and enhances its performance advantage as the number of events increases, especially compared to the baseline.

The addition of the 3D reconstruction allows for the most significant reduction in angular error of 82 % at higher event counts. However, adding our 'twin' approach allows for a further slight improvement of 7.2 % in angular accuracy.

3.4. Zoom function

The previously discussed adapted back-projection methods, including the 3D reconstruction, twin addition, and twin multiplication algorithms, have refined angular error and improved localization precision. They do so with a relatively uniform computational demand. The zoom function emerges as a solution to the challenge of reducing computation times, a critical aspect in scenarios where rapid data processing is paramount. This section delves into the zoom function's impact on computational efficiency. Note that our results demonstrate that utilizing the zoom function does not compromise accuracy compared to direct calculations with the final accuracy.

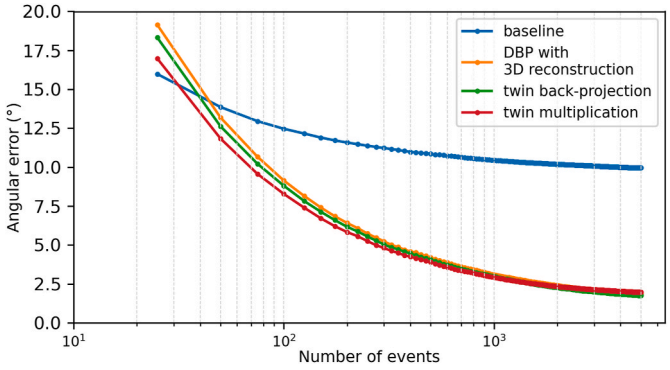

Fig. 16. Comparative analysis of median angular error across adapted back-projection methods. This figure aggregates the performance of all adapted back-projection methods by displaying the median angular error as a function of the number of events used. Each line represents the median error calculated across the dataset of 529 measurements for a specific method, allowing for a direct comparison of their accuracy and efficiency in varying conditions.

Table 2 enumerates the processing times and corresponding ratios for a series of zoom sequences used in imaging algorithms. Each zoom sequence represents a hierarchical approach to refining the analysis, starting from a wide zoom angle and progressively narrowing to 1°. The processing time is recorded in seconds (s), and the ratio is a comparative metric with the 1° zoom sequence set as the benchmark at 100.

Our test showed that performing the $30° > 5° > 1°$ zoom sequence was the fastest (0.45 s), meaning that first, back-projection is performed on a projection sphere with $30° \times 30°$ segments, then it is enhanced to 5° accuracy for the pixel of interest. As a final step, 1° accuracy was used around the pixel of interest in the 5° accuracy map. This zoom sequence allowed to perform the calculations 163 times faster than directly back-projecting with an accuracy of the projection sphere of 1° (73.4 s). This implementation significantly contributes to expeditiously and precisely determining gamma-ray source locations within our methodology. Applying the zoom function to gamma-ray source localization optimizes computational efficiency without compromising the precision and accuracy achieved.

3.5. Comparison with literature state of the art

This section compares the proposed approach for gamma-ray source localization to state-of-the-art techniques reported in the literature. It highlights any trade-offs between the precision and computational efficiency of the methods' performance. A comparison with the caliste HD detector is made based on the research of G. Daniel et al. [11,14].

A comparison was made with their back-projection algorithm, the SOE-RR algorithm, and their neural network. MLEM, another known reconstruction algorithm, was not included in the comparison. This exclusion is because the application of MLEM leads to poor performance with the Caliste system, primarily because of the uncertainties arising from the geometrical configuration of the single planar 2D detector [11, 14].

Webplot digitizer [16] was used to extract data from their research figures. Fig. 17 compares the angular error to the number of events used in the algorithm. The results show that CNN outperforms the presented algorithms regarding angular error for the same number of reconstructed events. However, Fig. 17 does not consider the measurement time needed to gather the events used in the back-projection algorithm.

In our research and the paper from G. Daniel et al., the sources are measured at a 30 cm source-to-detector distance. Therefore, the measurement time is normalized to the time it would take (hours) to measure a 1 MBq source of ^{137}Cs. Fig. 18 shows a similar scatterplot but using the normalized measuring time.

The analysis in Fig. 18 focuses on evaluating the performance of various reconstruction algorithms over a common operational

Table 2
Processing times and efficiency ratios for various zoom sequences in imaging algorithms. This table details the processing time required for different hierarchical zoom sequences and their efficiency compared to the 1° zoom benchmark. Ratios below 100 signify increased processing efficiency, with lower values indicating higher efficiency. The results demonstrate the impact of the zoom sequence strategy on the computational speed of image analysis.

Zoom sequence	Process time (s)	Ratio
1°	73,4	100
5 > 1°	0,89	1,21
20° > 1°	0,63	0,86
20° > 5° > 1°	0,49	0,67
30° > 5° > 1°	0,45	0,61
60° > 20° > 5° > 1°	0,57	0,78

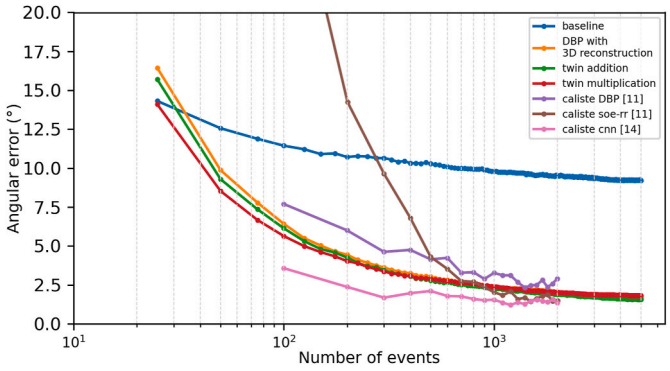

Fig. 17. Impact of event count on angular error in adapted back-projection methods. This figure demonstrates how the angular error varies with the number of events utilized in the back-projection process for each adapted method. The y-axis quantifies the total number of events, reflecting the data input size and computational load. At the same time, the x-axis represents the number of events.

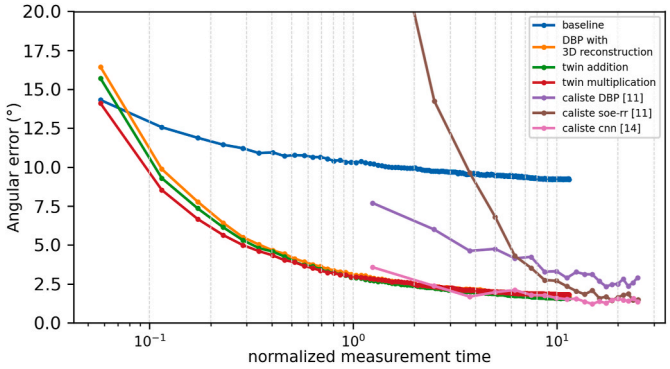

Fig. 18. Comparative analysis of angular error across adapted back-projection methods. This figure illustrates the angular error between the back-projection adaptations and the true source location as a function of normalized measurement time. Each curve represents a reconstruction method, showcasing their performance in accurately localizing the source over varying measurement durations. The y-axis quantifies the angular error, while the x-axis denotes the normalized measurement time of the detector, facilitating the evaluation of each method's efficiency and precision.

timeframe, specifically between 1.2 and 9.2 h. The evaluation metrics included the mean error, standard deviation, and range of errors to assess the precision and consistency of each algorithm under comparable conditions.

The Caliste CNN [14], our twin multiplication, and twin addition exhibited similar performance with notably low mean angular errors of 2.18°, 2.08°, and 1.95°, respectively. These algorithms also demonstrated low to moderate variability in their performance, as indicated by their standard deviations (0.66, 0.26, and 0.28), highlighting their robustness and reliability.

In contrast, our baseline algorithm recorded a higher mean angular error of 9.53°. Similarly, Caliste SOE-RR [11] presented the highest mean error of 10.38° and significant variability (standard deviation of 10.09), suggesting its performance may depend on longer measurement times and be less reliable under varying operational conditions.

This time-specific comparative analysis highlights the performance disparities among the presented algorithms. The presented algorithms can compete with state-of-the-art CNN algorithms tested on the Caliste HD system and outperform the SOE-RR algorithm.

We did not have the same dataset or processor available; therefore, to compare the processing time of the algorithms, it is assumed that the time needed for back-projection is equal (when using the same hardware, the number of events, and the accuracy of the projection sphere). Table 3 compares different algorithms based on their processing time ratios. The Baseline method is also used for baseline processing time, which is set as a benchmark with a ratio of 1. This ratio is a comparative measure against which the efficiency of other algorithms is assessed.

Table 3
Processing time ratios of various imaging reconstruction algorithms. This table outlines the relative processing times of several algorithms, with DBP serving as the reference standard. Ratios above 1 indicate longer processing times than DBP, while ratios below 1 denote shorter times. The data illustrates the trade-off between processing time and algorithm complexity or depth of analysis.

Algorithm	Processing time ratio
Baseline	1
Twin addition	1
Twin multiplication	1.01
Iterative zoom sequence (30°>°5 > 1°)	0.0062
DBP (caliste)	1
CNN (caliste)	1.02
SOE-RR (caliste) 20 000 iterations	25.7

Although the CNN does not add a lot of computational overhead (about 2 %), Its performance in terms of angular error is on par with our twin addition algorithm to which our zoom sequence can be applied. This allows to speed up the processing 163 times.

In robotics, particularly when onboard processing is a requirement, selecting an imaging reconstruction algorithm must prioritize efficiency without compromising accuracy. The Iterative Zoom Sequence's capability to maintain accuracy while drastically reducing processing time makes it an exemplary choice for such applications.

By employing the Iterative Zoom Sequence, robotic systems could achieve higher operational efficiencies, enabling them to perform more complex tasks in real time, a crucial advantage in applications ranging from industrial automation to autonomous navigation.

3.6. Enhancement of localization precision through wiener deconvolution

Like [17,18], Wiener deconvolution is applied to further refine the spatial resolution and precision. This approach aims to improve the effective image resolution quantified by the FWHM.

However, in the current study, a Gaussian point spread function (PSF) is employed instead of spherical harmonics to simplify the initial modeling aspects of Wiener deconvolution in our image reconstruction efforts. The Gaussian PSF was chosen due to its well-understood behavior and analytical simplicity. This approach allows for a baseline evaluation of the deconvolution process without requiring a comprehensive investigation into the PSF.

Applying Wiener deconvolution led to a noteworthy improvement in the FWHM of the detected gamma-ray sources. Before deconvolution, the FWHM stood at 50°, reflecting the system's resolution using direct back-projection methods. Post-deconvolution, a reduction in FWHM to 23° is observed, indicating a substantial enhancement in the system's ability to resolve closely spaced radiological sources while keeping computational demand low. The Wiener filter was applied in just 0.013 s. This enhancement in image resolution can aid in decommissioning scenarios where precise localization of radiation sources is paramount for safety and efficacy.

4. Discussion

Our aim is to locate sources as quickly as possible; therefore, our approach handles event selection differently. Instead of limiting the selected cones to forward scattered events, our research introduces twin addition and multiplication to limit the noise introduced by selecting faulty cones during event selection. An investigation was performed to determine the number of successfully estimated cones. Using the

measurement where the source is located at 0° azimuthal, 0° elevation angle, our approach generated 11582, of which 5332 cones overlap with the hotspot (46 %). When adhering to the same event selection rules proposed in G. Daniel et al. 's research [14], 6283 cones would have been created for our detector geometry. Of this number, only 2009 cones overlap with the hotspot (32 %).

For our detector geometry, the reconstruction of both cones allowed for the generation of 2.65 times more cones that overlap with the hotspot in the same measurement time.

An important aspect of our evaluation involves understanding the sources of error. The errors can differ for each cone or event depending on the measured energy, distance between interactions, etc. These errors can be attributed to two main factors: the uncertainty in energy measurement and the geometry of the sensor pixels.

The uncertainty caused by energy measurement impacts the scatter angle. For scatter angles ranging between 20° and 110°, this uncertainty remains below 0.2° FWHM, as calculated through reference [17]. However, for smaller or larger scattering angles, this uncertainty increases to about 0.8° FWHM for a scattering angle of 4° or 155°.

The geometry of the sensor introduces another source of error. This uncertainty is, among other factors, dependent on the location of the interactions and the distance between the scatter and absorption interaction points. For interactions occurring at the longest diagonal distance within the sensor, the uncertainty is below 0.1°. In contrast, for the shortest possible distance scenario—where one pixel is hit, an adjacent pixel is not, followed by another hit pixel—the uncertainty increases to about 0.7° FWHM, as calculated through reference [18]. To simplify the calculation, the spatial resolution was assumed to be isotropic and set to 55 μm, which is the pixel pitch. These geometric uncertainties are critical to consider as they can influence the accuracy of the reconstructed cones and axes.

Future work should focus on a better selection of events; early elimination of faulty cones might reduce noise in the back-projected heatmap. For example, machine learning may allow for better event selection, or adding a second back-projection step where faulty cones are eliminated might reduce noise in the back-projected image.

Deconvolution and the PSF in Timepix3-based single-layer Compton cameras need further investigation. This might further improve image resolution and FWHM while keeping computational demand low. Additionally, our research focuses on point sources. While this provides a solid foundation, applying the proposed methodology to extended sources requires further investigation. Enhancing the PSF will improve source localization accuracy and enable more effective differentiation between point sources and extended sources. This will be particularly beneficial in real-world applications where radiation sources often do not conform to idealized point-like distributions.

During previous research, it was shown that filtered back-projection in Compton imaging, enhanced through a Wiener filter derived from spherical harmonics, can provide improvements in the image resolution. This approach was tested using the OrionUM pixelated CdZnTe imaging spectrometer, which offered higher resolution with lower computational costs than traditional iterative methods. An experiment with two ^{228}Th sources demonstrated the method's effectiveness, with the filtered image showing a significantly improved FWHM compared to direct back-projection. This methodology underscores the potential for refined radiological imaging processes, promising enhanced accuracy [19,20].

5. Conclusion

The inherent risks associated with traditional decommissioning practices — particularly the exposure of human operators to harmful radiation —underscore the urgent need for alternative solutions. Our research responds to this need by optimizing a technology that minimizes human risk while ensuring comprehensive and accurate radiological assessments.

In addressing this critical challenge, our study has introduced an approach that significantly enhances the precision and efficiency of gamma-ray source localization. By optimizing event selection criteria for Compton camera events and harnessing the capabilities of an optimized back-projection method integrated with a novel single-layer Compton camera and 3D camera setup, we have delineated a path toward safer, more accurate, and more efficient decommissioning operations.

In this study, we have demonstrated an approach to enhancing the precision and efficiency of gamma-ray source localization by developing and implementing an optimized back-projection method. Our methodology leveraged the capabilities of the Timepix3 readout chip within our Compton camera setup to facilitate a more accurate and efficient mapping of gamma-ray sources. Adding 3D reconstruction to the Compton imaging data allowed for a reduction in angular error of 82 % at higher event count, while the introduction of 'twin addition' and 'twin multiplication' techniques offered an additional improvement of 7.2 %. In particular, the twin approach allowed for better handling of data ambiguities, thereby enhancing the overall reliability of the localization process. Additionally, implementing a zoom function improved computational efficiency up to 163 times. It maintained accuracy, demonstrating its potential as a valuable tool for optimizing gamma-ray source localization tasks, making it well-suited for integration onto mobile robotic platforms.

Our comparative analysis revealed that this approach not only surpasses the baseline method in terms of accuracy but also holds a competitive edge over contemporary state-of-the-art methods, including those deployed in the Caliste-HD detector. This validation against the latest advancements in the field highlights the robustness and potential of our methodology.

Looking forward, the focus should be on further refining algorithmic enhancements and exploring their integration with autonomous or semi-autonomous robotic platforms. Such developments could significantly mitigate human exposure to radiation and streamline decommissioning processes. Moreover, exploring machine learning for event selection in Compton cameras or filtered back-projection techniques could offer new horizons for improving localization precision and image resolution.

Additionally, further research should concentrate on extended sources and the PSF, which is crucial for accurately identifying extended radiation sources. This research has primarily utilized point sources; however, understanding and refining the PSF will enhance the capability to detect and characterize extended sources, which are prevalent in decommissioning environments.

CRediT authorship contribution statement

Mattias Simons: Writing – review & editing, Writing – original draft, Visualization, Validation, Software, Resources, Project administration, Methodology, Investigation, Funding acquisition, Formal analysis, Data curation, Conceptualization. **Anouk Michiels:** Writing – review & editing, Visualization, Validation, Software, Methodology, Investigation, Formal analysis, Data curation, Conceptualization. **Jan Genoe:** Writing – review & editing, Supervision, Resources, Project administration, Conceptualization. **Wouter Schroeyers:** Writing – review & editing, Supervision, Project administration, Funding acquisition.

Declaration of competing interest

The authors declare no conflicts of interest regarding the publication of this manuscript. The research presented in this paper was conducted with academic and scientific integrity. There are no financial, personal, or professional relationships that could be perceived as potential conflicts of interest. This manuscript has not been submitted to any other journal for simultaneous consideration. We confirm that this work is original and has not been published elsewhere.

Acknowledgment

This work was also supported by the Fund for Scientific Research Flanders [Fonds Wetenschappelijk Onderzoek (FWO)] scholarship nr 1SA2621N and 1SA2623N hosted by UHasselt.

The computational resources and services used in this work were provided by the VSC (Flemish Supercomputer Center), funded by the Research Foundation - Flanders (FWO) and the Flemish Government.

This research was performed in the context of the ARCHER sproject. The archer project was carried out by academic research partners UHasselt and KU Leuven in collaboration with the industrial partners EQUANS and Magics Instruments. This project is funded by the Energy Transition Fund of the FOD economy (federal government Belgium). The publication exclusively contains the opinions of the authors. The General Directorate Energy is not liable for any use of the information in the current paper.

During the preparation of this work, the author(s) used ChatGPT to improve the readability of the introduction and methods section. After using this tool/service, the author(s) reviewed and edited the content as needed and take(s) full responsibility for the publication's content.

References

[1] R. Volk, F. Hübner, T. Hünlich, F. Schultmann, The future of nuclear decommissioning – a worldwide market potential study, Energy Pol. 124 (Jan. 2019) 226–261.
[2] J. Kaulard, B. Brendebach, Radiation Protection during Decommissioning of Nuclear Facilities – Experiences and Challenges, vol. 70, 2005, pp. 14–24.
[3] R. Pavlovsky, et al., 3-D Radiation Mapping in Real-Time with the Localization and Mapping Platform LAMP from Unmanned Aerial Systems and Man-Portable Configurations, Dec. 2018.
[4] M.S. Lee, M. Hanczor, J. Chu, Z. He, N. Michael, R. Whittaker, 3-D Volumetric Gamma-Ray Imaging and Source Localization with a Mobile Robot, Feb. 2018.
[5] D. De Schepper, I. Dekker, M. Simons, L. Brabants, W. Schroeyers, E. Demeester, Towards a semi-autonomous robot platform for the characterisation of radiological environments, SSRR 2022 - IEEE Int. Symp. Safety, Secur. Rescue Robot (2022) 230–237.
[6] L. Brabants, M. Simons, D. De Schepper, Minimal detection time for localisation of radioactive hotspots in low and elevated background environments , using a CZT gamma-ray spectrometer Minimal detection time for localisation of radioactive hotspots in low and elevated background environments, Nucl. Technol. 208 (11) (2022) 1681–1695.
[7] D. De Schepper, A. Melnikov, M. Simons, L. Brabants, W. Schroeyers, E. Demeester, Design and Comparison of a Passive and Active Multiple Radiological Point Source Localisation Algorithm, IROS (2022).
[8] D. De Schepper, M. Simons, W. Schroeyers, K. Kellens, and E. Demeester, "Learning multiple radiation source distribution models using Gaussian processes," 56th International Symposium on Robotics (ISR Europe). (2023).
[9] M. Simons, D. De Schepper, E. Demeester, W. Schroeyers, Localization of hotspots via a lightweight system combining Compton imaging with a 3D lidar camera, Nucl. Eng. Technol. 56 (2024) 3188–3198.
[10] O. Klein, T. Nishina, Über die Streuung von Strahlung durch freie Elektronen nach der neuen relativistischen Quantendynamik von Dirac, Z. Phys. 52 (11–12) (Nov. 1929) 853–868.
[11] G. Daniel, O. Limousin, D. Maier, A. Meuris, F. Carrel, Compton imaging reconstruction methods: a comparative performance study of direct back-projection, SOE, a new Bayesian algorithm and a new Compton inversion method applied to real data with Caliste, EPJ Web Conf. 225 (2020) 06006.
[12] A. Andreyev, A. Sitek, A. Celler, Fast image reconstruction for Compton camera using stochastic origin ensemble approach, Med. Phys. 38 (1) (2011) 429–438.
[13] A. Andreyev, A. Celler, I. Ozsahin, A. Sitek, Resolution recovery for Compton camera using origin ensemble algorithm, Med. Phys. 43 (8) (2016) 4866–4876.
[14] G. Daniel, Y. Gutierrez, O. Limousin, Application of a deep learning algorithm to Compton imaging of radioactive point sources with a single planar CdTe pixelated detector, Nucl. Eng. Technol. 54 (5) (2022) 1747–1753.
[15] T. Poikela, et al., Timepix3: a 65K channel hybrid pixel readout chip with simultaneous ToA/ToT and sparse readout, J. Instrum. 9 (5) (2014).
[16] A. Rohatgi, Webplotdigitizer: Version 4.7, 2024.
[17] C.E. Ordonez, A. Bolozdynya, W. Chang, Dependence of angular uncertainties on the energy resolution of Compton cameras, Proc. IEEE Nucl. Sci. Symp. Med. Imaging Conf. (1998) 1122–1125.
[18] E. Ordonez, W. Chang, A. Bolozdynya, Angular uncertainties due to geometry and spatial resolution in compton cameras, IEEE Trans. Nucl. Sci. 46 (4 PART 2) (1999) 1142–1147.
[19] J. Chu, M. Streicher, J.A. Fessler, Z. He, Unbiased filtered back-projection in 4π compton imaging with 3D position sensitive detectors, IEEE Trans. Nucl. Sci. 63 (6) (Dec. 2016) 2750–2756.
[20] L.C. Parra, Reconstruction of cone-beam projections from Compton scattered data 1, IEEE Trans. Nucl. Sci. 47 (4 PART 2) (2000) 1543–1550.